J Mater Sci (2009) 44:6167–6181
DOI 10.1007/s10853-009-3854-4

Effect of H_2S on Fe corrosion in CO_2-saturated brine

E. Abelev · J. Sellberg · T. A. Ramanarayanan · S. L. Bernasek

Received: 23 May 2009 / Accepted: 27 August 2009 / Published online: 10 September 2009

Abstract The effect of H_2S at ppm level concentrations on iron corrosion in 3 wt% NaCl solutions saturated with CO_2 in the temperature range of 25–85 °C is examined using electrochemical and surface science techniques. Small H_2S concentrations (5 ppm) have an inhibiting effect on corrosion in the presence of CO_2 at temperatures from 25 to 55 °C. At 85 °C, however, 50 ppm H_2S is needed to provide significant corrosion inhibition. At higher H_2S concentrations, the corrosion rate increases rapidly, while still remaining below the rate for the H_2S-free solution. Characterization of the iron surfaces after corrosion was carried out using X-ray photoelectron spectroscopy and X-ray diffraction. A sulfur peak (S2p) is observed at a binding energy of 161.8 eV in all cases, attributable to disulfide (S_2^{2-}) formation. Corrosion protection in the temperature range 25–55 °C can be attributed to Fe(II) bonded to S and O. At 85 °C, protection of the iron surface is most likely due to FeS_2 formation. Morphological changes on the iron surface after exposure to H_2S containing solutions were observed by SEM. A thin protective film was seen after exposure to solutions containing 5 ppm H_2S at 25 °C, while at 85 °C, with the addition of 50 ppm H_2S to CO_2-saturated brine solution, a dense protective film was formed on the iron surface.

E. Abelev · J. Sellberg · T. A. Ramanarayanan · S. L. Bernasek (✉)
Department of Chemistry, Princeton University, Princeton, NJ 08544-1009, USA
e-mail: sberna@princeton.edu

Introduction

In the search for new sources of oil and gas, operational activities have moved to harsher environments in deeper high-pressure/high-temperature wells and remote offshore locations. This has created increased challenges to the economy of project development and execution where operational integrity and accurate prediction of materials performance are becoming paramount. In addition, the economic move toward multi-phase transportation through sub-sea completions and long infield flow lines has increased the risk of corrosion.

Corrosion, therefore, remains a major operational obstacle to successful hydrocarbon production, and its optimum control and management is regarded essential for the cost-effective design of facilities and their safe operations. This has wide ranging implications on the integrity of many materials used in the petroleum industry. Oilfield corrosion manifests itself in several forms among which CO_2 corrosion (sweet corrosion) and H_2S corrosion (sour corrosion) in the produced fluids and oxygen corrosion in water injection systems are by far the most prevalent forms of attack encountered in oil and gas production. The majority of oilfield failures result from CO_2 corrosion of carbon and low alloy steels primarily due to inadequate knowledge and predictive capability and the insufficient resistance of carbon and low-alloy steels to this type of attack [1–5]. The understanding, prediction, and control of corrosion are key challenges to sound facilities design, operation, and subsequent integrity assurance.

CO_2 corrosion, or "sweet corrosion," of carbon and low-alloy steels is not a new problem. It was first recorded in the U.S. oil and gas industry in the 1940s, followed by several studies since then [5–8]. The mechanisms of carbon dioxide corrosion of steel in oil and gas fields are complex.

Two effects of CO_2 have been reported [9–15]: (i) more intense cathodic evolution of hydrogen than would be expected from the acidity of the solution and (ii) the formation of carbonate films at the anodic metal surface. The first effect is associated with the buffering properties of carbonic acid [9, 10, 13, 15], while the second is associated with the low solubility of iron carbonate [9–14]. It has been shown [16] that carbonic acid solutions are more corrosive to carbon steel than solutions of the stronger acids (e.g., HCl) at the same pH value, since the latter exhibit no buffering effect.

Two viewpoints exist when considering cathodic processes related to CO_2 corrosion of carbon steel in oil and gas field environments [11–15]. One view assumes that in the presence of CO_2, it is the H_3O^+ cations generated near the cathode that are mainly reduced, while buffering carbonic acid serves as their source. According to the second view, carbonic acid itself (or, at elevated temperatures, HCO_3^- ions) serves as a proton carrier [8–15, 17]. Homogeneous, heterogeneous, and mixed depolarization mechanisms are involved [9–22]:

$$HCO_{3\ sol}^- + e^- \rightarrow H_{ads} + CO_3^{-2} \quad (1)$$

$$HCO_{3\ near-el}^- + H_{ads} + e^- \rightarrow H_2 \uparrow + CO_3^{-2} \quad (1a)$$

$$H_2CO_{3\ sol} + e^- \rightarrow H_{ads} + HCO_{3\ ads}^- \quad (2)$$

Carbonic acid is subsequently regenerated [10] by:

$$HCO_{3\ ads}^- + H_3O_{near-el}^+ \rightarrow H_2CO_3 + H_2O \quad (3)$$

In actuality this means that carbonic acid combines the functions of a buffer and a carrier for discharging proton [9, 11, 17, 19–22].

Carbonate films play an important role in carbon dioxide corrosion. In the presence of $FeCO_3$ films, the corrosion rate depends on the composition and structure of the films. The protective properties of $FeCO_3$ are primarily determined by the temperature and the pH of the medium [9–14, 19–23]. These films exhibit rather poor protective characteristics at pH < 7 while at higher pH values exceeding 7, better protective tendencies are shown [9, 15].

According to the literature [11, 24], the corrosion mechanism of carbon steel changes between 40 and 60 °C. The corrosion rate at the higher T is determined by formation of a siderite surface film ($FeCO_3$). At $T < 60$ °C, the anodic formation of $FeHCO_3^+$ and the cathodic discharge of H_2CO_3 (at pH < 5) are the limiting heterogeneous steps. The resulting porous films exhibit little protective effect.

At $T > 60$ °C, a dense film is formed, thus altering the rate limiting step [11]. The corrosion rate now is controlled by the solubility and permeability of thin $FeCO_3$ films which are pH-dependent. With a decrease in pH, the corrosion rate increases. However, this dependence is ambiguous. Iron carbonate can form either on the metal surface or as a precipitate from solution. In the former case, its formation includes several steps, the number and sequence of which depend on the pH of the medium [9, 11, 12]. These steps have been described in detail in reported studies [9, 15]. At $T > 100$ °C, the fraction of iron carbonate in the corrosion products is reduced, while the content of magnetite, Fe_3O_4, increases [11]. Such a mixed film can also offer corrosion protection.

H_2S corrosion or sour corrosion is especially of concern in gas production wells having H_2S concentrations in excess of about 0.5 pct. H_2S dissolves in the chloride-containing produced water present in the wells: the metal–water–hydrogen sulfide system is complex and a wide variety of compounds can form. Depending on the pH of the electrolyte, sulfur can be present in three different forms; H_2S, HS^- and S^{2-}. The pH of brine saturated with H_2S is ~4 [25] at room temperature. At this pH value H_2S is the dominating species (>99.9%) in solution.

The proposed reactions that occur when H_2S is present in the system are as follows [26]:

$$H_2S_{(g)} \Leftrightarrow H_2S_{(aq)} \quad (4)$$

$$H_2S_{(aq)} \Leftrightarrow H^+ + HS_{(aq)}^- \Leftrightarrow 2H^+ + S_{(aq)}^{2-} \quad (5)$$

Accordingly, hydrogen ion reduction is assumed to be the most dominant cathodic reaction in H_2S corrosion.

Among the many proposals for H_2S corrosion, one mechanism for iron dissolution in aqueous solutions containing H_2S [27, 28] is as follows:

$$Fe + H_2S + H_2O \Leftrightarrow FeSH_{ads}^- + H_3O^+ \quad (6)$$

$$FeSH_{ads}^- \Leftrightarrow Fe(SH)_{ads} + e^- \quad (7)$$

$$Fe(SH)_{ads} \Leftrightarrow FeSH^+ + e^- \quad (8)$$

The species FeSH at the electrode surface could be incorporated directly into a growing layer of mackinawite, $FeS_{(1-x)}$, [29] according to the following reaction:

$$FeSH^+ \rightarrow FeS_{(1-x)} + xSH^- + (1-x)H^+ \quad (9)$$

If reaction (9) leads to local supersaturation of $FeS_{(1-x)}$ at the electrode surface, nucleation and growth of the mackinawite phase occurs on the surface. In addition to mackinawite, many other sulfide phases such as troilite, pyrrhotite (iron deficient sulfide) and pyrite can form as corrosion products on the surface of steel [30–33]. The protective nature, its morphology (amorphous or polycrystalline), and the composition of the corrosion product depend on the pH, the concentration of H_2S in the solution and the temperature. At lower values of pH (<2), iron is dissolved and iron sulfide is not precipitated on the surface of the metal due to a very high solubility [34–36] of iron sulfide in such solutions. At pH values from 3 to 5, an

inhibitive effect of H_2S is seen as FeSH species may form mackinawite via reaction (9). The metastable mackinawite can convert into other forms of sulfides which are more protective such as troilite, and the protective or inhibitive effect of H_2S depends on the stability and compactness of the transformed sulfide [27]. At higher pH values between 6 to 8.8 it was found that sulfide formed was most unprotective, with mackinawite being the main corrosion product [32].

In general, a compact sulfide phase provides corrosion protection while a porous phase is unprotective. Highly defective films formed especially at high H_2S concentrations can be unprotective [29]. Especially at the higher temperatures, even a compact sulfide surface phase such as pyrrhotite is unprotective in view of the fast diffusion of iron ions through it [30, 37].

Transition from sweet to sour corrosion

Many sweet wells gradually become sour because of the formation of H_2S by the action of sulfate-reducing bacteria. The influence of H_2S on CO_2 corrosion varies with the H_2S concentration [2, 38–44]. Low levels of H_2S have been reported to affect CO_2 corrosion in different ways. H_2S can either increase the CO_2 corrosion rate by acting as a promoter of anodic dissolution through sulfide adsorption and affecting the pH or it can retard the sweet corrosion rate by the formation of a protective sulfide film [44, 45]. Thus, oil and gas installations could experience lower corrosion rates under slightly sour conditions compared to completely sweet systems. In addition, H_2S can play a significant role in the type and properties of the corrosion films formed, either improving or undermining them [46].

Many papers have been published on the interaction of H_2S with low-carbon steels [1, 2, 40, 41, 47, 48]. However, literature data on H_2S-steel interaction in the presence of CO_2 are less extensive since the nature of the interaction is complex. Videm et al. [39] and Mishra et al. [38] have reported two opposing results concerning the H_2S effect. While the former study suggests that very small amounts (<30 ppm) of H_2S in CO_2-containing water increase the corrosion rate, the latter has argued that small amounts of H_2S have some inhibitive effect on CO_2 corrosion of steels. They attributed this observation to the formation of an iron sulfide film that was apparently more protective than $FeCO_3$. Nevertheless, it must be emphasized that H_2S can also form a non-protective layer and accelerate the anodic dissolution of steel.

Studies on the effect of very small H_2S concentrations on CO_2 corrosion at low pH, where precipitation of iron sulfides does not occur, have been reported [42–44]. The data strongly suggest that the presence of very small amounts of H_2S ($\sim$10 ppm) leads to a significant reduction of iron corrosion rate in CO_2 environments. At higher H_2S concentrations (above 10 ppm) this trend is arrested and somewhat reversed. The effect seems to depend largely on the H_2S concentration, since data obtained under different conditions follow the same trend [42]. However, the exact role of H_2S was not clarified in a fundamental sense.

Temperature has a strong influence on the iron corrosion reactions occurring on the surface. Temperature can accelerate all the processes involved in CO_2 and H_2S corrosion including transport of species, chemical reactions in the bulk solution and electrochemical reactions at the metal surface. Depending on whether the solubility of protective films (such as iron carbonate or other salts) is exceeded, temperature can either increase or decrease the corrosion rate [49, 50]. Saridisco and Pitts studied the corrosion of iron in an H_2S–CO_2–H_2O system [32, 33]. They concluded that during liquid phase corrosion of iron by H_2S–CO_2–H_2O, the overall reaction is controlled partially by interface reaction and partially by diffusion of ions and electrons across the surface film. At low H_2S concentrations, the reaction mechanism approaches complete diffusion control and at high H_2S concentrations it approaches complete interface control. Murata et al. [51] evaluated the corrosion rate as a function of H_2S and CO_2 partial pressure and temperature. Lichti et al. [52] have reviewed the experience with geothermal wells in New Zealand that produce brines containing CO_2 and H_2S. They found the formation of corrosion products containing mackinawite, troilite and pyrrhotite. They concluded that sulfide films reduced corrosion rates, even when present in minute amounts. Later, Smith and Miller [53] presented the results of laboratory tests that were run to evaluate the minimum H_2S levels required to form mackinawite. In a Norwegian study, it was shown that the effect of H_2S on CO_2 corrosion is significant only in the low pH range (pH < 5) [54]. Recent studies of the morphology of iron sulfide films formed in aqueous H_2S/CO_2 environments indicate that the nature of the sulfide films affects the efficiency of added corrosion inhibitors [55]. However, the reasons behind the H_2S effect on CO_2 corrosion are not fully clarified.

Thus, the current study focuses on developing a more detailed understanding of the nature of the "H_2S effect" on CO_2 corrosion in the temperature range between 25 and 85 °C. We have used pure iron as a model for corrosion of carbon steels and recognize that there may be differences, particularly localized and pitting corrosion that may occur on mild steel, which are not likely to be an issue with pure iron samples. Our main goal is to study in detail the surface chemistry and the initial stages of iron corrosion in CO_2-saturated solutions upon addition of low levels of H_2S. What is the influence of temperature on the corrosion

process? A combination of electrochemical and surface spectroscopic studies was used, the former to quantify the rates of corrosion and the latter to establish the chemistry and morphology of the surface under specific exposure conditions.

Experimental

Iron samples were cut from a high purity (99.98%), polycrystalline iron rod (Electronic Space Products International (ESPI)). Disk-shaped samples of 15 mm diameter and 1.5 mm thickness were polished on one side with silicon carbide paper down to 1200 grit. This was followed by washing the sample in DI water (18.2 MΩ·cm, milliQ) and drying in high purity nitrogen.

Electrochemical measurements were carried out in a standard three-electrode electrochemical cell [25] to estimate the corrosion characteristics of Fe. The reference electrode was a standard calomel electrode (SCE); the counter electrode consisted of a pair of graphite rods connected by a copper wire, while the working electrode was the iron disk sealed inside a Teflon casing with ~ 1 cm^2 of the "test" surface exposed to the aqueous medium.

Experiments were conducted at room temperature and at elevated temperatures of 55 and 85 °C at atmospheric pressure. The working electrode was introduced after passing CO_2 containing the appropriate concentration of H_2S through the electrolyte solution for 60 min. A steady flow of the gas mixture was maintained throughout the experiment. The concentration of H_2S in CO_2 was controlled by gas mass flow rate controllers and gas mixers. Electrochemical impedance spectroscopic (EIS) measurements were carried out using a Solartron Model 1287 Potentiostat/Galvanostat with Solartron Model 1250 lock-in amplifier. The instrument was controlled by a PC operated by the electrochemistry software, CorrView2, from Scribner Associates. A single sinusoidal potential of 10 mV peak-to-peak was superimposed on the open-circuit potential over the frequency range of 10^{-2} to 6.5×10^6 Hz. The experimental frequency was scanned from the higher to the lower value. Nyquist and Bode plots were obtained for each experiment and the polarization resistance, R_p (inversely proportional to the corrosion rate), was determined by fitting the curves to a proposed equivalent circuit.

Nyquist plots were observed to be complete but depressed semicircles. Several factors can cause such depression: roughness of surface oxide layers [56], the inhomogeneous reaction rate on the electrode surface [57] or the varying thickness of surface layers [56]. The Nyquist data were fitted using the equivalent circuit shown in the insert of Fig. 1a. The equivalent circuit consists of the uncompensated solution resistance, R_s, charge transfer resistance, R_{ct}, and electrode capacitance, C. The non-ideal capacitive characteristics of the electrochemical interface were described by the constant phase element (CPE), which was used instead of double layer capacitance in the presented equivalent circuit. The use of a constant phase element is a representation of non-ideal behavior caused by the roughness of the corrosion product layer [56]. The impedance of the CPE is given by Eq. 10:

$$Z_{CPE} = A(j\omega)^{-n} \tag{10}$$

where Z_{CPE} is the impedance of the CPE, A is a proportionality constant, $j = \sqrt{-1}$, $\omega = 2\pi f$ and n is the extent of phase shift ($0.5 \leq n \leq 1$), with $n = 1$ corresponding to a pure capacitive element [56].

EIS was carried out over a period of 24 h until a steady state was reached. In all the cases presented above there is a variation of the polarization resistance (R_p) with time to reach a constant value over a period of 24 h. According to the Stern-Geary equation, R_p is inversely proportional to the corrosion rate [25].

$$i_{corr} = \left(\frac{1}{R_p}\right)\frac{\beta_A\beta_C}{2.3(\beta_A + \beta_C)} \tag{11}$$

$$\text{Corrosion rate (mpy)} = \frac{(0.13)\cdot i_{corr}\text{EW}}{d} \tag{12}$$

where β_A, β_C are Tafel constants (mV/decade of current), R_p is polarization resistance (Ω·cm^2), EW is equivalent weight of corroding species (g), d is density of the corroding species (g/cm^3), and i_{corr} is the corrosion current density (μA/cm^2).

Once a constant R_p value was attained, the iron samples were removed from the electrochemical cell, washed in DI water, dried and then transferred to an ultra high vacuum (UHV) system. X-ray photoelectron (XPS) spectra were measured with a VG Scientific ESCALAB2 spectrometer equipped with an Al Kα radiation source ($hv = 1486.6$ eV) and a hemispherical analyzer connected to a three-channel detector. During the measurements the base pressure in the chamber was around 1×10^{-9} Torr. Measurements were carried out at normal take-off angle, $\theta = 90°$, between the sample surface and the direction of photoelectrons detected by the analyzer. Spectra were detected at a constant pass energy of 20 eV. The peaks corresponding to different species present on the metal were assigned to the respective bonding states through the standard curve fitting procedure. The spectra were corrected based on the position of adventitious carbon at 285.0 ± 0.1 eV. Curve fitting of the core-level XPS lines was carried out by CASA XPS software with a Gaussian–Lorentzian product function and non-linear Shirley [56] background subtraction. An asymmetric tail function was introduced for the Fe 2p region to obtain the best possible fit.

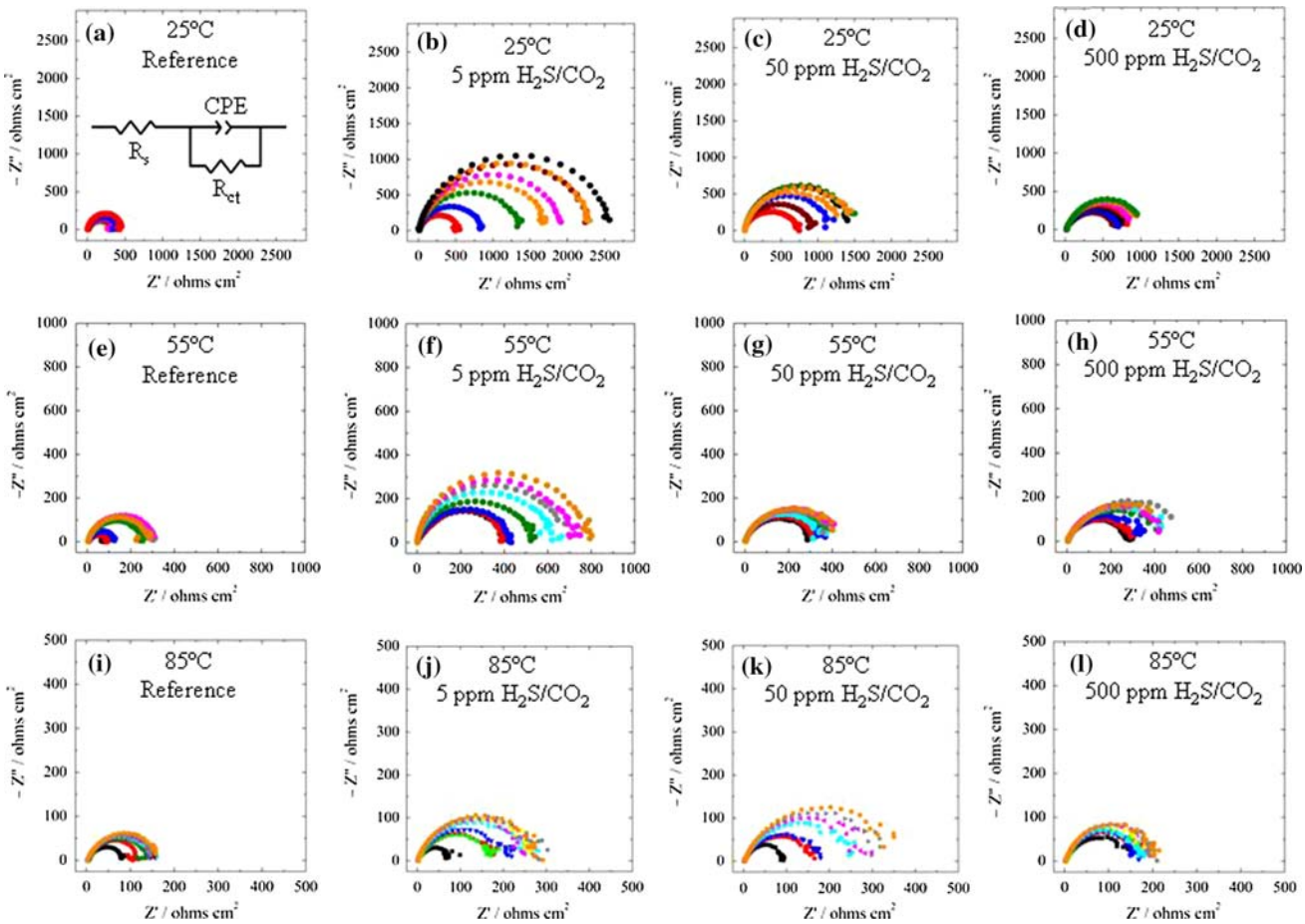

Fig. 1 Nyquist plots of the iron sample during 24 h exposure to CO_2-saturated 3 wt% NaCl solution containing **a** 0 ppm, **b** 5 ppm, **c** 50 ppm, **d** 500 ppm H_2S at 25 °C, **e** 0 ppm, **f** 5 ppm, **g** 50 ppm, **h** 500 ppm H_2S at 55 °C and **i** 0 ppm, **j** 5 ppm, **k** 50 ppm, **l** 500 ppm H_2S at 85 °C. The equivalent electrical circuit used for modeling is shown in **a**

X-ray diffraction (XRD) analysis was conducted using a Bruker D8 Focus diffractometer employing Cu Kα radiation ($\lambda = 1.5406$ Å). XRD spectra were used to identify different phases present in the thin film of corrosion products formed on iron exposed to the aqueous environment at different temperatures of study.

The morphological changes of the iron samples after 24 h exposure were examined using a Philips XL30 FEG SEM.

Results and discussion

Impedance study

The corrosion behavior of iron exposed to CO_2-saturated brine solutions containing low H_2S concentrations at room temperature and elevated temperatures was studied in the temperature range 25–85 °C, using EIS. Figure 1 presents a set of Nyquist impedance plots obtained from the iron electrode immersed for 1, 2, 4, 8, 16, 20, and 24 h in CO_2-saturated 3 wt% NaCl solution at 25 °C containing (a) 0 ppm, (b) 5 ppm, (c) 50 ppm, and (d) 500 ppm H_2S at OCP (open circuit potential), at 55 °C containing (e) 0 ppm, (f) 5 ppm, (g) 50 ppm, and (h) 500 ppm H_2S, and at 85 °C containing (i) 0 ppm, (j) 5 ppm, (k) 50 ppm, and (l) 500 ppm H_2S. R_p values extracted from the impedance curves were used to estimate the extent of corrosion protection upon H_2S addition. The equivalent circuit shown as an inset in Fig. 1a was used to fit the experimental impedance data for the determination of R_p.

A comparison of the data at 25, 55 and 85 °C in Fig. 1 shows that for the H_2S-free CO_2-saturated 3 wt% NaCl solutions, the R_p value is much higher at 25 °C than at 55 and 85 °C, indicating a higher corrosion rate at the higher temperatures as expected. With the addition of 5 ppm H_2S to the CO_2-saturated solution at 25 °C, the R_p value undergoes a significant increase from 485 Ω·cm^2 for the H_2S-free solution to 2650 Ω·cm^2 for the 5 ppm H_2S case. At higher H_2S concentrations, 50 and 500 ppm, the semicircles become smaller indicating lower R_p values than in the 5 ppm H_2S case, but still higher than the H_2S-free

situation. At 55 °C the highest R_p value, 792 Ω·cm^2, was obtained for the solution containing 5 ppm H_2S as in the 25 °C case. However, at 85 °C the highest R_p value was obtained for the solution containing 50 ppm H_2S. Thus, the H_2S concentration needed to achieve maximum corrosion protection is a function of temperature.

Figure 2 presents the time dependence of the reciprocal polarization resistance, $1/R_p$, of the iron sample during 24 h exposure to CO_2-saturated 3 wt% NaCl solutions with and without addition of H_2S at (a) 25 °C, (b) 55 °C and (c) 85 °C. Each point in Fig. 2 was calculated from the equivalent circuit shown in Fig. 1 with R_p equal to R_{ct}. In all cases, the reciprocal R_p values are observed to decrease with time and reach a plateau in approximately 24 h. The existence of such a plateau was confirmed for up to 72 h of corrosion. Since the reciprocal R_p values are proportional to the rate of corrosion (Eqs. 11 and 12), these results indicate that after an initial decrease, the rate of corrosion attains a constant value. The lowest $1/R_p$ value or corrosion rate in the 25 and 55 °C cases was obtained after addition of 5 ppm H_2S to CO_2-saturated 3 wt% NaCl solution, while at the higher temperature, 85°C, the lowest corrosion rate was obtained after addition of 50 ppm H_2S to solution.

Figure 3 summarizes the $1/R_p$ values as a function of H_2S concentration at three different temperatures; 25, 55 and 85 °C. As can be seen, at 25 and 55 °C, there is a minimum in the $1/R_p$ versus H_2S concentration graph corresponding to 5 ppm H_2S concentration at which maximum corrosion protection is observed. At the higher temperature of 85 °C, the minimum in the $1/R_p$ values shifted to 50 ppm H_2S in the solution. The changes in the nature of reaction layers on the Fe surface at the different temperatures and H_2S concentrations should explain the observed differences in corrosion behavior.

As was mentioned earlier, the reciprocal of R_p is proportional to the corrosion rate. The temperature

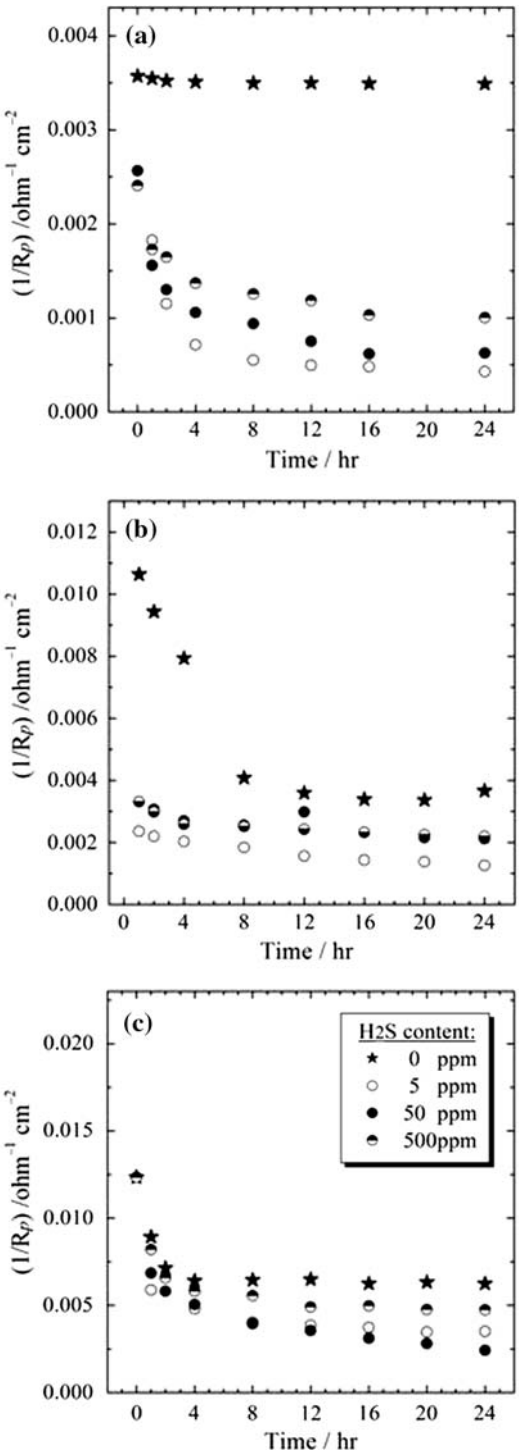

Fig. 2 Time dependence of the polarization resistance, R_p, of an iron sample during 24 h exposure to CO_2-saturated 3 wt% NaCl solution at **a** 25 °C, **b** 55 °C and **c** 85 °C

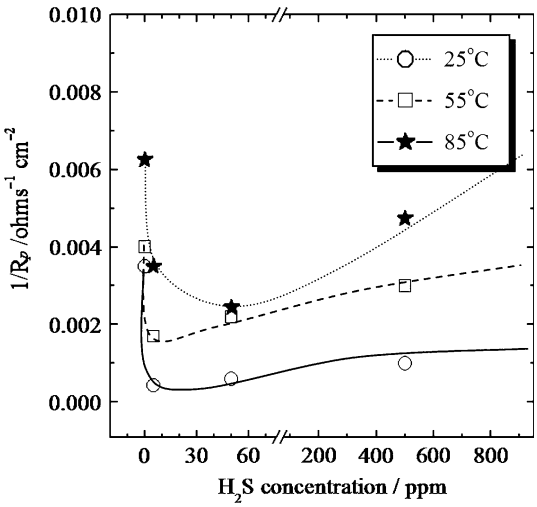

Fig. 3 Inverse of R_p (measure of corrosion) as a function of H_2S concentration in CO_2-saturated 3 wt% NaCl solution at 25, 55 and 85 °C

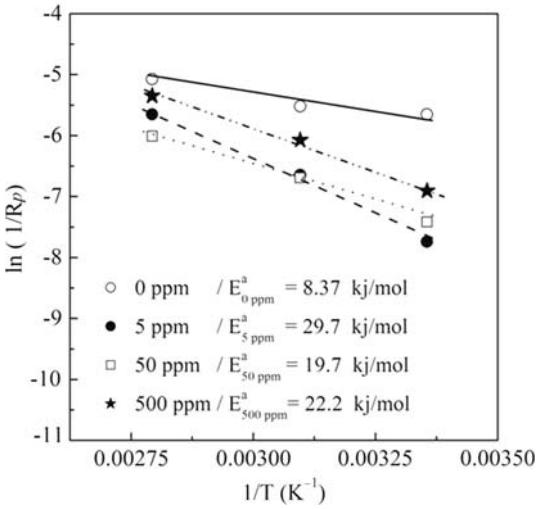

Fig. 4 Arrhenius plot of the corrosion rate for Fe exposed to CO_2-saturated 3 wt% NaCl solution containing 0, 5, 50 and 500 ppm H_2S

dependence of $1/R_p$ (Fig. 4) is in accordance with the Arrhenius equation. The activation energy calculated from Fig. 4 is 8.4 kJ/mol for iron corrosion in CO_2-saturated brine, which is reasonable for the fast charge transfer process [30]. With the addition of 5 ppm H_2S in the CO_2-saturated 3 wt% NaCl solution, the activation energy increased to a value of 30.5 kJ/mol. At 50 and 500 ppm H_2S the activation energy values were 21.8 and 23.4 kJ/mol, respectively. These values are within the range reported in the literature for charge transfer processes (12.6–41.8 kJ/mol) [30] and as such, charge transfer rather than any solid state diffusion step is implicated as the main corrosion mechanism.

Surface characterization

X-ray photoelectron spectroscopy study

In order to understand the role of H_2S on the inhibition of iron corrosion in CO_2-saturated media, sulfur bonding with iron was examined using high-resolution XPS. Iron samples were removed from the aqueous environment after 24 h when a steady state was reached, washed with DI water and immediately transferred to a UHV chamber for XPS characterization.

Figure 5 shows high-resolution spectra for (a) $Fe2p_{3/2}$, and (b) O1s and (c) S2p regions for an iron sample exposed for 24 h to CO_2-saturated 3 wt% NaCl solution at 25 °C containing 5, 50 and 500 ppm H_2S. The prominent Fe^0 peak indicates that the surface film is thin enough to allow photoelectrons originating from the bulk metal (see Fig. 5a) to be detected. Curve fitting in Fig. 5a shows that both Fe^2 and Fe^3 species are present on the surface, which can be attributed to different iron oxide (Fe_3O_4), hydroxide ($Fe(OH)_2$ and sulfide (Fe(II)-S or Fe(II)-O-S) present. The binding energy values for Fe^0, Fe^{+2} and Fe^{+3} peaks are in agreement with the literature values [56–65].

Figure 5b shows the O1s signal which was fitted to three peaks. The first peak at 529.7 ± 0.1 eV corresponded to

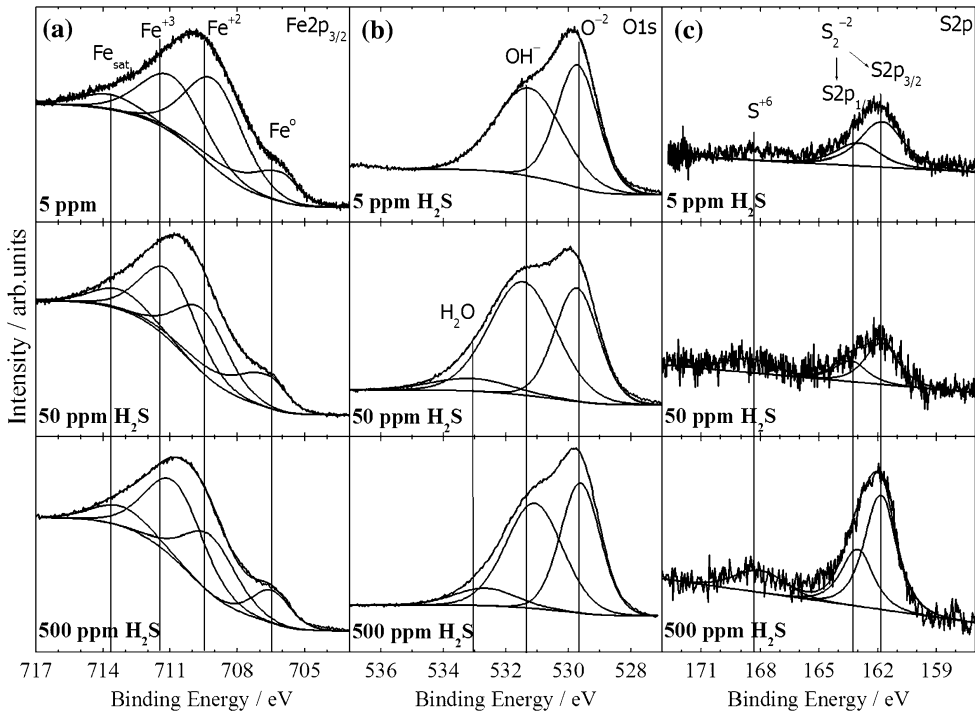

Fig. 5 Comparison of the high-resolution XP spectra of **a** $Fe2p_{3/2}$, **b** O1s and **c** S2p of the iron sample after 24 h exposure to CO_2-saturated 3 wt% NaCl solution containing 5, 50 and 500 ppm H_2S at 25 °C

oxygen in the oxide form (O^{2-}) [63–71]. The other peaks at 531.4 ± 0.1 eV and 533.35 ± 0.15 eV corresponded to OH^- [62–69] and some adsorbed water possibly picked up during sample transfer to the UHV environment.

Figure 5c shows the S2p signal. The S2p spectra for the 5 ppm H_2S case (top curve) were fitted using doublets for the $2p_{3/2}$ and $2p_{1/2}$ separated by a spin–orbit splitting of 1.2 eV [69, 70]. The $S2p_{1/2}$ peak area was constrained to be half the area of the $S2p_{3/2}$ peak. The spectra were resolved into two components: $S2p_{3/2}$ at 161.7 eV and $S2p_{1/2}$ at 162.9 eV, the location of the peaks can be interpreted as the disulfide (S_2^{2-}) [64, 65]. It should be stressed that the exact peak location is between the monosulfide (S^{2-}) located at 161.4 ± 0.4 eV [64, 69–74] and disulfide (S_2^{2-}) located at 162.3 ± 0.2 eV [64, 69–74]. At higher H_2S concentrations (50 and 500 ppm), the S2p peak was obtained at the same binding energies but with higher intensity, due to the higher amount of sulfur on the surface. An additional S2p peak was obtained at 168.5 ± 0.1 eV which could be assigned to S^{+6} arising from environments containing SO_4^{2-} [65, 67, 68, 70]. Formation of SO_4^{2-} species may be due to partial oxidation of iron corrosion products in air during sample transfer. All the fitting parameters have been listed in Table 1 including peak positions, FWHM (full width at half maximum) and line shape. The first column lists various species present on the surface. The error bar associated with peak position definition measurements was ±0.2 eV.

The main difference in the S2p spectrum between the 5, 50 and 500 ppm H_2S cases was the FWHM of the $S2p_{3/2}$ and $S2p_{1/2}$ peaks; as H_2S concentration increased the FWHM of the $S2p_{3/2}$ and $S2p_{1/2}$ peaks narrowed. At 5 ppm H_2S the FWHM of $S2p_{3/2}$ and $S2p_{1/2}$ peaks was 2.4 eV while at 500 ppm H_2S it was 1.76 eV. These observations can be attributed to a transformation from adsorbed sulfur on the surface at 5 ppm H_2S concentration to a compact iron-sulfide or iron-oxy-sulfide compound on the surface at 500 ppm H_2S concentration. There is evidence in the literature to suggest that adsorbed specie have broader XPS peaks than compact compounds [65, 66].

Similar surface characteristics were obtained for the 55 °C case, as seen in Fig. 6 and Table 2. The S2p peak locations were 161.74 ± 0.2 eV for $S2p_{3/2}$ and 162.9 ± 0.2 eV for $S2p_{1/2}$. An additional S2p peak was observed at 167.8 ± 0.1 eV which could be assigned to S^{+6} arising from environments containing SO_4^{2-} [64–76]. FWHM narrowing of the S2p peak from 2.5 to 1.85 eV was observed as in the case at 25 °C, again suggesting a transition from adsorbed sulfur on the surface at 5 ppm H_2S to the formation of a more crystalline compound at higher H_2S concentrations. The main difference in the 55 °C case as compared to the 25 °C case is a significant decrease in the concentration of Fe^{+2} species on the iron surface (Fig. 6a).

Table 1 Deconvolution parameters for fitting the S2p, O1s and $Fe2p_{3/2}$ XPS peaks measured for the iron surface exposed to CO_2-saturated 3 wt% NaCl solution containing 5, 50 and 500 ppm H_2S at 25 °C

H_2S (ppm)	25 °C			
		Position (eV)	FWHM (eV)	Line shape
5	$S2p_{3/2}$	161.7	2.4	GL(80)T(3)
	$S2p_{1/2}$	162.9		
	O1s	529.7	1.54	GL(30)
		531.3	2.5	GL(30)
	$Fe2p_{3/2}$	706.07	1.85	GL(30)T(0.95)
		709	3	GL(30)
		710.9	3.3	GL(30)
		713.7	3	GL(30)
50	$S2p_{3/2}$	161.73	1.83	GL(80)T(3)
	$S2p_{1/2}$	163.2		
	S2p	168.7	3	GL(30)
	O1s	529.73	1.65	GL(30)
		531.5	2.5	GL(30)
		533.2	3	GL(30)
	$Fe2p_{3/2}$	706.7	2	GL(30)T(0.95)
		709.6	2.7	GL(30)
		711.06	2.9	GL(30)
		713.3	3	GL(30)
500	$S2p_{3/2}$	161.79	1.76	GL(80)T(3)
	$S2p_{1/2}$	162.9		
	S2p	168.8	3	GL(30)
	O1s	530.2	1.5	GL(30)
		531.4	2.2	GL(30)
		533.5	2.2	GL(30)
	$Fe2p_{3/2}$	706.5	2	GL(30)T(0.95)
		709.05	2.7	GL(30)
		711.5	3	GL(30)
		713.9	3	GL(30)

Figure 7 shows the high-resolution spectra of the (a) S2p, (b) O1s and (c) $Fe2p_{3/2}$ regions for an iron sample exposed for 24 h to CO_2-saturated 3 wt% NaCl solution at 85 °C containing 5, 50 and 500 ppm H_2S. As in the 25 and 55 °C cases, the S2p spectra were fitted using doublets for the $2p_{1/2}$ and $2p_{3/2}$ separated by a spin–orbit splitting of 1.2 eV [69, 70]. The spectra were split into two components: $S(2p_{3/2})$ at 161.75 ± 0.2 eV and $S(2p_{1/2})$ at 162.95 ± 0.2 eV, the location of the peaks was interpreted as the disulfide (S_2^{2-}) [64, 68–74]. The main change in the S2p spectrum for the 5, 50 and 500 ppm H_2S cases was again the FWHM of the $S2p_{3/2}$ and $S2p_{1/2}$ peaks. At 5 ppm H_2S the FWHM of $S2p_{3/2}$ and $S2p_{1/2}$ peaks was 2.2 eV

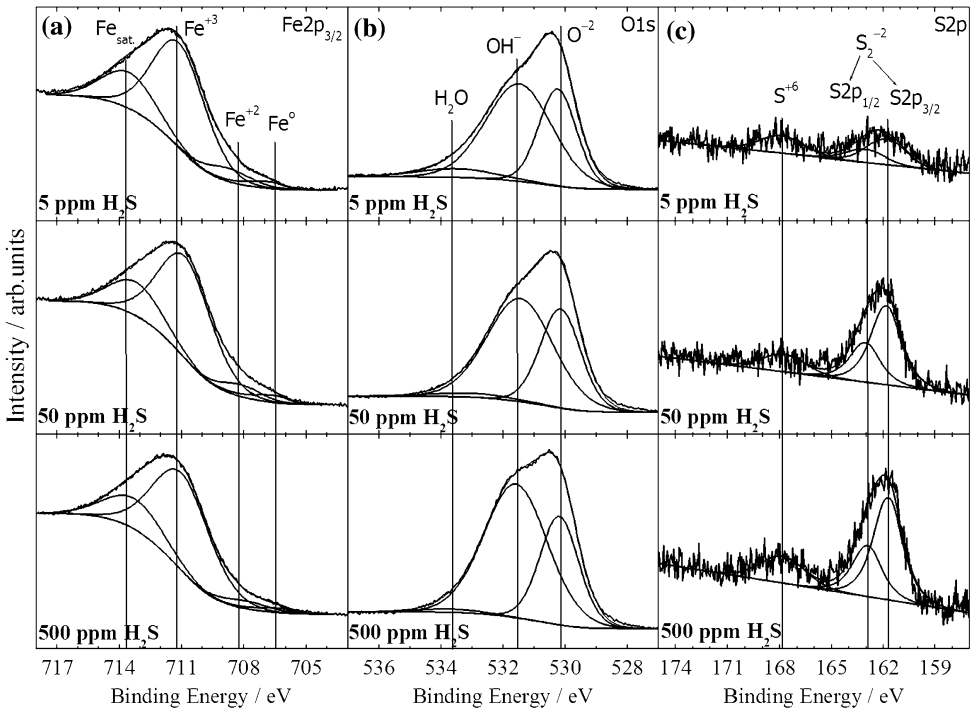

Fig. 6 Comparison of the high-resolution XP spectra of **a** $Fe2p_{3/2}$, **b** O1s and **c** S2p of the iron sample after 24 h exposure to CO_2-saturated 3 wt% NaCl solution containing 5, 50 and 500 ppm H_2S at 55 °C

while at 50 ppm H_2S it narrowed to 1.5 eV, and at higher H_2S concentration (500 ppm) the $S2p_{3/2}$ and $S2p_{1/2}$ peaks broadened again to 2.04 eV. It was argued earlier that narrowing of the peak is due to a change from adsorbed sulfur on the surface to a more compact compound phase [75, 76]. Thus, at 5 ppm H_2S the amount of adsorbed sulfur on the surface is insufficient to provide significant protection of the iron surface. It is likely that between 5 and 50 ppm, there exists an H_2S level at which there is complete coverage of the surface by adsorbed sulfur, thus leading to much higher corrosion resistance. At 50 ppm H_2S an iron sulfide compound (FeS) becomes the predominant species on the surface and provides excellent corrosion protection. With further increase to 500 ppm H_2S, a less protective FeS_2 forms and covers the iron surface (Table 3).

The O1s signal was deconvoluted into two main peaks. The first peak at 530.3 ± 0.1 eV corresponded to oxygen in the oxide form (O^{2-}) [64–71]. The second peak at 531.6 ± 0.1 eV corresponded to iron carbonate [64, 70]. An additional peak was observed at 533.6 ± 0.1 eV which most likely arises from adsorbed water picked up during sample transfer to the UHV environment.

The analysis of the $Fe2p_{3/2}$ peaks revealed very low intensity Fe^0 peak, the peak at 708.9 ± 0.2 eV (Fig. 7a) which corresponds to Fe^{+2}, and a peak at 711.1 ± 0.2 eV assigned to iron-carbonate [70]. The presence of Fe^{+2} species on the iron surface indicates Fe(II)-S compound formation [70]. It should be stressed that iron carbonate was present in the 5, 50 and 500 ppm H_2S cases. The $Fe^{+2}_{sulfur}/Fe^{+2}_{carbonate}$ intensity ratio was 0.16 for 5 ppm H_2S, 0.18 for 50 ppm and 0.06 for 500 ppm H_2S. The 50 ppm H_2S case corresponds to the largest amount of FeS_2 on the iron surface. Corrosion protection is also the highest for this case.

X-ray diffraction

XRD analysis was carried out on the iron sample after 24 h exposure in CO_2-saturated 3 wt% brine solution at 85 °C. It should be noted that XRD analysis was performed on all the samples, however, due to the formation of thin films at 25 and 55 °C, surface compound identification was not possible by XRD for these samples. Figure 8a presents the XRD spectra of iron corrosion products after 24 h exposure in CO_2-saturated H_2S-free solution at 85 °C. As one can see iron corrosion products mainly consist of $FeCO_3$ with traces of Fe_3O_4 and iron-hydroxides (FeOOH and $Fe(OH)_3$). With the addition of 50 ppm H_2S (Fig. 8b) to CO_2-saturated 3 wt% NaCl solution, the corrosion products were mainly FeS_2, $FeCO_3$, Fe_3O_4 and FeOOH. These results point to the formation of FeS_2 as the reason for iron corrosion protection at 85 °C.

SEM study

The morphology of the iron surface exposed for 24 h at OCP (open circuit potential) in CO_2-saturated 3 wt% NaCl

Table 2 Deconvolution parameters for fitting the S2p, O1s and $Fe2p_{3/2}$ XPS peaks measured for the iron surface exposed to CO_2-saturated 3 wt% NaCl solution containing 5, 50 and 500 ppm H_2S at 55 °C

H_2S (ppm)	55 °C			
		Position (eV)	FWHM (eV)	Line shape
5	$S2p_{3/2}$	161.74	2.5	GL(80)T(3)
	$S2p_{1/2}$	162.9		
	S2p	167.9	3	GL(30)
	O1s	530.24	1.5	GL(30)
		531.5	2.5	GL(30)
		533.5	3	GL(30)
	$Fe2p_{3/2}$	706.8	1.5	GL(30)T(0.95)
		708.72	2.5	GL(30)
		711.12	3.	GL(30)
		713.55	3	GL(30)
50	$S2p_{3/2}$	161.78	1.9	GL(80)T(3)
	$S2p_{1/2}$	163.98		
	S2p	167.8	3	GL(30)
	O1s	530.16	1.52	GL(30)
		531.45	2.5	GL(30)
		533.1	3	GL(30)
	$Fe2p_{3/2}$	706.5	1.5	GL(30)T(0.95)
		708.13	2.25	GL(30)
		710.8	3	GL(30)
		713.2	3	GL(30)
500	$S2p_{3/2}$	161.66	1.85	GL(80)T(3)
	$S2p_{1/2}$	162.86		
	S2p	167.8	3	GL(30)
	O1s	530.19	1.5	GL(30)
		531.6	2.4	GL(30)
		533.7	2.4	GL(30)
	$Fe2p_{3/2}$	706. 3	1.5	GL(30)T(0.95)
		708.2	2.25	GL(30)
		711	3.3	GL(30)
		713.3	3	GL(30)

solution at 25, 55 and 85 °C with addition of 5, 50 and 500 ppm H_2S was investigated by SEM. Figure 9 presents SEM micrographs after 24 h exposure of iron to CO_2-saturated 3 wt% NaCl solution at 25 °C, with different H_2S concentrations. As can be seen, localized regions of severe corrosion were observed on the exposed surface at 25 °C in CO_2-saturated H_2S-free solution (Fig. 9a, b). Corrosive degradation reveals grain boundaries clearly just like an etched surface. Images at higher magnifications (Fig. 9b) reveal active dissolution of iron from within the grains. These results are consistent with the high corrosion rates observed by electrochemical techniques (EIS, Fig. 1a). The addition of 5 ppm H_2S to the environment (Fig. 9c, d) leads to a dramatic change in the morphology of the iron surface. No dissolution of the iron surface was detected at low magnification (Fig. 9c). At higher magnification (Fig. 9d) some small regions of dissolution could be observed on the scratch marks left from polishing, but in general the surface was much smoother and no grain dissolution or pitting corrosion was detected. At higher H_2S concentrations, 50 ppm (Fig. 9e, f) and 500 ppm (Fig. 9g, h), a completely different morphology of the iron surface was obtained. Small grains of 1–2 μm could be observed which are not seen in the H_2S-free case or the 5 ppm H_2S case. This observation further strengthens the suggestion that at high H_2S concentrations at room temperature (above 50 ppm) a transformation takes place leading to the formation of FeS_2 from previous iron oxides or hydroxides.

Figure 10 presents SEM micrographs after 24 h exposure of iron to CO_2-saturated 3 wt% NaCl solution at 55 °C, with different H_2S concentrations. The results are similar to the 25 °C case; localized regions of severe corrosion were observed on the exposed surface at 55 °C in CO_2-saturated H_2S-free solution (Fig. 10a, b). The addition of 5 ppm H_2S (Fig. 10c, d) leads to a dramatic change in the iron surface morphology. No local regions of corrosion on the iron surface were detected (Fig. 10c, d). At higher H_2S concentrations; 50 ppm (Fig. 10e, f) and 500 ppm (Fig. 10g, h), grain boundary dissolution is seen. Also, the precipitation of surface phases is evident.

Figure 11 presents SEM micrographs after 24 h exposure of Fe to CO_2-saturated 3 wt% NaCl solution at 85 °C, with different H_2S concentrations. At 85 °C the situation is somewhat different, for the reference sample (CO_2-saturated 3 wt% NaCl solution) active iron dissolution is observed. Corrosive degradation reveals grain boundaries and some precipitates are clearly seen on the surface (Fig. 11b). The chemical composition of the corrosion products, mainly $FeCO_3$ with small amounts of FeOOH, was characterized by XRD. Images at higher magnifications (Fig. 11b) reveal a thick porous corrosion product morphology. The addition of 5 ppm H_2S to the environment (Fig. 11c, d) did not lead to significant change in the morphology of the iron surface. Active dissolution of iron can still be seen, grain boundaries are revealed and at higher magnification, dissolution of iron inside the grains was also observed. The main difference in surface morphology for the 5 ppm H_2S case is that much less corrosion products are found on the iron surface, compared to the H_2S-free case. At higher H_2S concentration, 50 ppm, no dissolution of the iron surface was detected (Fig. 11e, f). The iron surface was covered by a dense film of corrosion products which were a mixture of FeS_2, $FeCO_3$ and FeOOH, as characterized by XRD. The inset in Fig. 11f shows the iron surface at higher magnification (×50,000). The

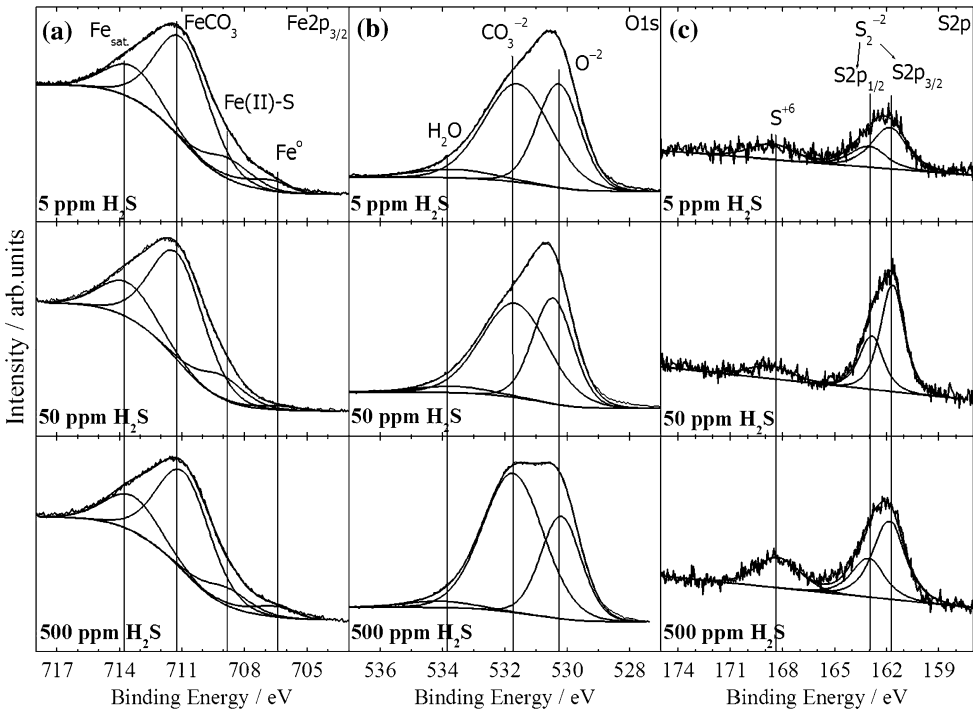

Fig. 7 Comparison of the high-resolution XP spectra of **a** Fe2p$_{3/2}$, **b** O1s and **c** S2p of the iron sample after 24 h exposure to CO_2-saturated 3 wt% NaCl solution containing 5, 50 and 500 ppm H_2S at 85 °C

protective corrosion product layer consisted of small circular grains, 100–200 nm in diameter. At higher H_2S concentrations, 500 ppm (Fig. 11g, h), a somewhat similar morphology of the iron surface was obtained as in the 50 ppm H_2S case. However, the corrosion layer is more porous in this case, small grains of 100–200 nm in diameter are formed but they are less dense than in the 50 ppm H_2S case. These results can explain the increased corrosion rates measured by EIS for the 500 ppm case (Fig. 1g, h).

Summarizing the XPS, XRD and SEM results the following mechanism for iron corrosion in low H_2S, CO_2-saturated brine is suggested. At low temperatures, in the 25–55 °C range, enhanced iron corrosion protection was achieved with relatively low H_2S concentrations (around 5 ppm), while at higher temperatures, ~85 °C, a higher content of H_2S was needed to provide maximum iron corrosion protection (around 50 ppm). This observation is attributed to the different mechanisms responsible for iron protection. At low temperatures, S^{2-} adsorption on iron, iron oxide or iron hydroxide provides iron protection at low (~5 ppm) H_2S concentrations. At higher H_2S concentrations (up to 500 ppm) a phase transformation occurs on the Fe surface, leading to a sulfur-rich compound which is less protective, most likely because of its low density and higher porosity. It should be stressed that such a surface compound still provides significant protection compared to the CO_2-saturated H_2S-free case. At 85 °C, unprotective iron carbonate formation was observed on the surface. At low H_2S concentrations (~5 ppm) sulfide ions adsorb partly on the $FeCO_3$ and partly on the exposed Fe. The concentration of H_2S is inadequate to provide sufficient sulfur coverage and corrosion inhibition. At 50 ppm H_2S excellent corrosion protection is achieved accompanied by the formation of a surface film of FeS_2. Most likely, the FeS_2 forms by a conversion of $FeCO_3$ upon reaction with H_2S. It is reasonable to suppose that an H_2S concentration exists between 5 and 50 ppm at which full surface coverage by adsorbed sulfide ions leads to excellent corrosion protection. At high H_2S concentrations of 500 ppm, no significant corrosion protection is observed. At this concentration, there is more complete conversion of $FeCO_3$ to FeS_2, leading to non-compact surface layers because of the volume change accompanying the conversion reaction.

Conclusions

The corrosion of iron in CO_2-saturated 3 wt% NaCl solutions containing small concentrations of H_2S has been studied in the 25–85 °C temperature range. Based on EIS studies iron develops pronounced corrosion protection in CO_2-saturated 3 wt% NaCl solution upon addition of 5 ppm H_2S in the temperature range 25–55 °C. As the H_2S concentration was increased to 50 ppm and to 500 ppm, the level of protection decreased. At a higher temperature of 85 °C, 50 ppm H_2S was needed to achieve maximum protection of the iron surface.

Table 3 Deconvolution parameters for fitting the S2p, O1s and $Fe2p_{3/2}$ XPS peaks measured for the iron surface exposed to CO_2-saturated 3 wt% NaCl solution containing 5, 50 and 500 ppm H_2S at 85 °C

H_2S (ppm)	85 °C			
		Position (eV)	FWHM (eV)	Line shape
5	$S2p_{3/2}$	161.75	2.2	GL(80)T(3)
	$S2p_{1/2}$	162.95		
	S2p	168.6	3	GL(30)
	O1s	530.28	1.6	GL(30)
		531.6	2.5	GL(30)
		533.6	3	GL(30)
	$Fe2p_{3/2}$	706.6	1.8	GL(30)T(0.95)
		708.7	2.5	GL(30)
		711	3.	GL(30)
		713.4	3	GL(30)
50	$S2p_{3/2}$	161.63	1.5	GL(80)T(3)
	$S2p_{1/2}$	163.8		
	S2p	168.7	3	GL(30)
	O1s	530.46	1.5	GL(30)
		531.7	2.5	GL(30)
		533.6	2.7	GL(30)
	$Fe2p_{3/2}$	706.17	1.8	GL(30)T(0.95)
		709	2.5	GL(30)
		711.2	3	GL(30)
		713.6	3	GL(30)
500	$S2p_{3/2}$	161.8	2.04	GL(80)T(3)
	$S2p_{1/2}$	162.98		
	S2p	168.3	3	GL(30)
	O1s	530.3	1.5	GL(30)
		532	2.4	GL(30)
		533.9	2.5	GL(30)
	$Fe2p_{3/2}$	706.4	1.8	GL(30)T(0.95)
		708.8	2.5	GL(30)
		710.9	3.0	GL(30)
		713.4	3.0	GL(30)

The surface-sensitive XPS technique combined with XRD was used to study the chemical states and composition of the iron surface exposed to CO_2-saturated 3 wt% NaCl solution containing different H_2S concentrations. At low temperatures (range 25–55 °C) with the addition of 5 ppm H_2S to CO_2-saturated 3 wt% NaCl solution, XPS surface characterization revealed Fe(II)-S and Fe(II)-O-S bond formation which led to pronounced corrosion protection. At higher temperatures (85 °C) the nature of the corrosion protection was different. The maximum corrosion protection was achieved upon addition of 50 ppm H_2S

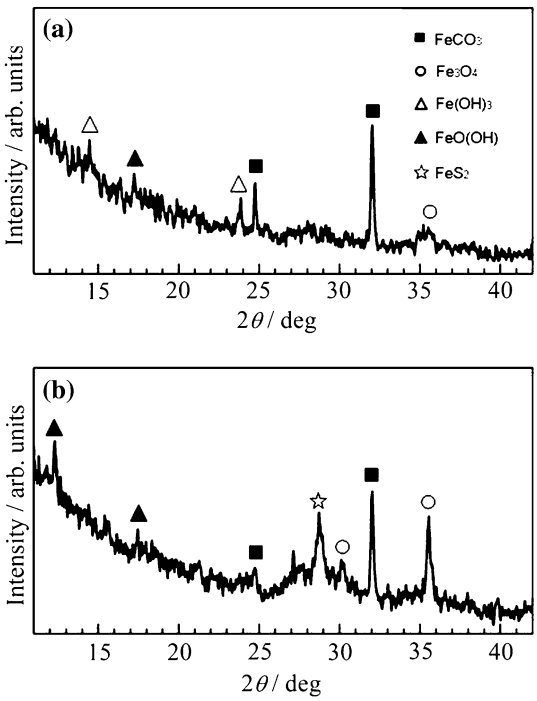

Fig. 8 XRD patterns of the Fe samples after 24 h exposure to CO_2-saturated 3 wt% NaCl solution containing **a** 50 and **b** 500 ppm H_2S at 85 °C

and the main corrosion products found on the iron surface were FeS_2, $FeCO_3$, Fe_3O_4 and FeOOH. Using SEM on the samples studied at 85 °C, a dense protective layer of FeS_2 was seen to form on the iron surface upon addition of 50 ppm H_2S to CO_2-saturated 3 wt% NaCl, while at higher concentrations of H_2S a less crystalline and less protective iron sulfide was observed to form on the surface.

A mechanism for iron corrosion and inhibition in H_2S/CO_2-containing brine at 25 and 85 °C was proposed. At 25 °C, with the addition of 5 ppm H_2S to CO_2-saturated brine solution, corrosion inhibition was attributed to adsorption of sulfur on the native iron oxide, and this layer provides significant corrosion inhibition. The main species responsible for inhibition include Fe(II) bonded to O and S. At higher H_2S concentrations a thicker layer of iron corrosion products forms on the surface by a dissolution-precipitation mechanism. This layer is porous and inhomogeneous, having voids and irregularities as shown by SEM, and is less protective than the adsorption layer that forms at 5 ppm H_2S. This layer consists of a mixture of iron oxide and sulfide phases and forms by conversion of oxide to sulfide. At 85 °C with the addition of 50 ppm H_2S to CO_2-saturated brine, corrosion inhibition was attributed to the formation of a dense protective film of FeS_2, $FeCO_3$ and Fe_3O_4.

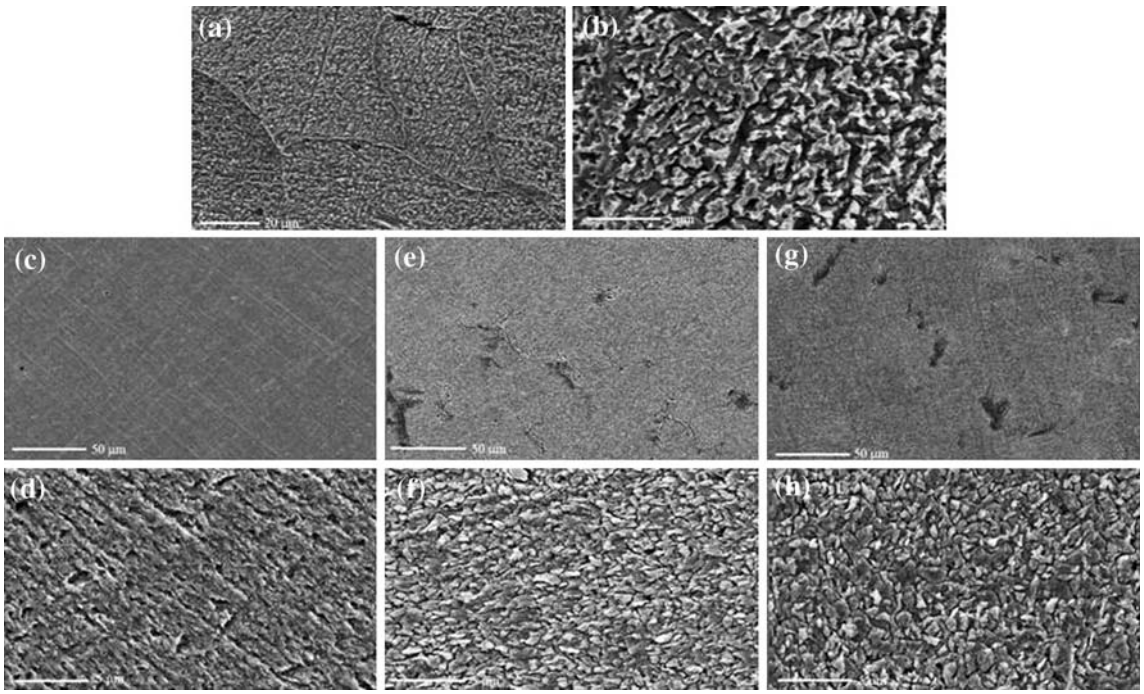

Fig. 9 SEM micrographs of the Fe samples after 24 h exposure to CO_2-saturated 3 wt% NaCl solution at 25 °C containing **a**, **b** 0, **c**, **d** 5, **e**, **f** 50 and **g**, **h** 500 ppm H_2S

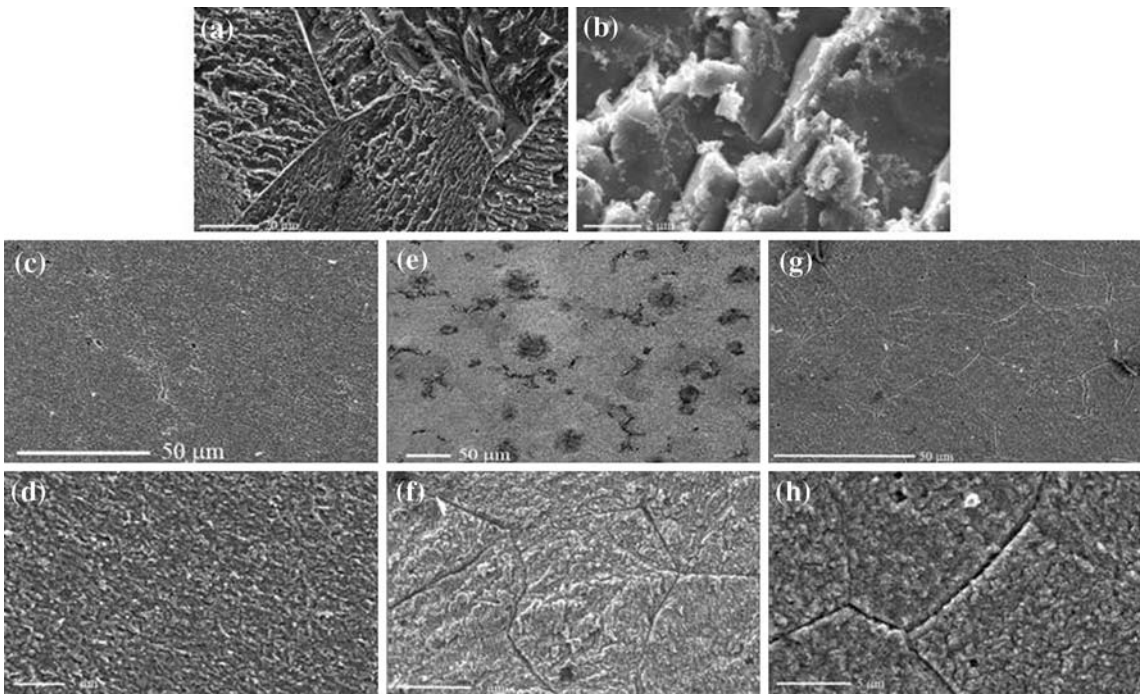

Fig. 10 SEM micrographs of the Fe samples after 24 h exposure to CO_2-saturated 3 wt% NaCl solution at 55 °C containing **a**, **b** 0, **c**, **d** 5, **e**, **f** 50 and **g**, **h** 500 ppm H_2S

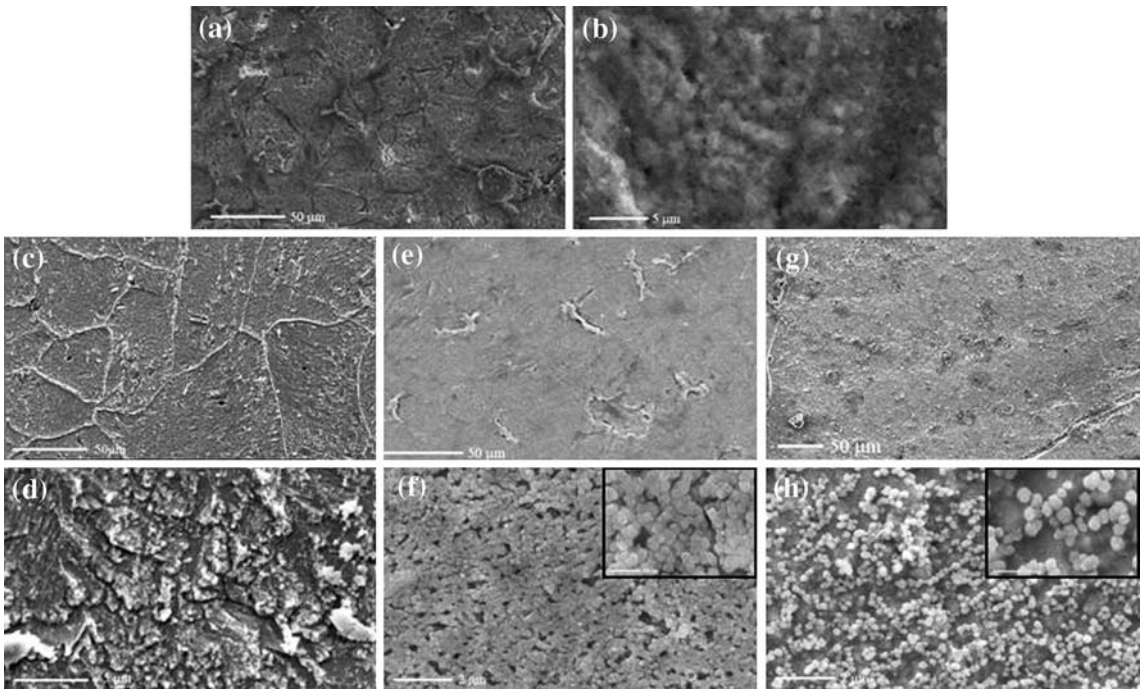

Fig. 11 SEM micrographs of the Fe samples after 24 h exposure to CO_2-saturated 3 wt% NaCl solution at 85 °C containing **a**, **b** 0, **c**, **d** 5, **e**, **f** 50 and **g**, **h** 500 ppm H_2S

Acknowledgement This work was partially supported by the National Science Foundation, Division of Chemistry, CHE-0616457.

References

1. Kermani MB, Harrop D (1996) SPE Production Facilities 11:186
2. Kermani MB, Morshed A (2003) Corrosion 59:659
3. McIntyre P (2002) Corros Manag 46:19
4. Bonis M, Thiam P, Eurocorr 2000, Conference of the European Federation of Corrosion
5. Schwenk W (1974) Werst Korros 25:643
6. de Waard C, Milliams DE (1975) Corrosion 31:177
7. Ogundele GI, White WE (1987) Corrosion 43:665
8. Crolet JL, Bonis MR (1983) Corrosion 39:39
9. Moiseeva LS (2005) Protection of materials, vol 41, pp 82–90
10. Magot M, Tardy C, Caumette P, Hurtevent C, Crolet JL (1993) 10th European Corrosion Congress, pp 576–580
11. Schmitt G (1984) Advances in CO_2 corrosion, vol 1. NACE, Houston, p 1
12. Crolet JL, Thevenot N, Nešić S (1996) CORROSION/96, paper no. 4. NACE, Houston, TX
13. Videm K, Dugstad A (1987) CORROSION/87, paper no. 42. NACE, Houston, TX
14. Videm K, Dugstad A (1989) Mater Perform 4:46
15. Moiseeva LS, Kuznetsov YI (1996) Zashch Met 32:513
16. Belevskii VS, Kudelin YI, Lisov SF, Timonin VA (1990) Fiz Khim Mekh Mater 6:16
17. De Waard C, Lotz U, Milliams DE (1991) Corrosion 47:976
18. Moiseeva LS, Tereshina RM (1994) Zashch Met 30:410
19. Dunlop AK, Hassell HL, Rhodes PR (1984) Advances in CO_2 corrosion, vol 1. NACE, Houston, p 52
20. De Waard C, Lotz U, Milliams DE (1991) CORROSION/91, paper no. 577. NACE, Houston, TX
21. Wieckowski A, Ghali E, Szklarczyk M, Sobkowski J (1983) J Electrochim Acta 28:1619
22. Ogundele GI, White WE (1986) Corrosion 42:71
23. French EC, Martin RL, Dougherty JA (1989) CORROSION/89, paper no. 435. NACE, Houston, TX
24. Kurahashi H, Kurisu T, Sone I, Wada K, Nakai I (1985) Corrosion 41:211
25. Bhargava G (2007) PhD dissertation, Princeton University
26. Banaś J, Lelek-Borkowska U, Mazurkiewicz B, Solarski W (2007) Electrochim Acta 52:5704
27. Ma H, Cheng X, Li G, Chen S, Quan Z, Zhao S, Niu L (2000) Corros Sci 42:1669
28. Wu X, Ma H, Chen S, Xu Z, Sui A (1999) J Electrochem Soc 146:1847
29. Shoesmith DW, Taylor P, Bailey MG, Owen DG (1980) J Electrochem Soc 127:1007
30. Vedage H, Ramanarayanan TA, Mumford JD, Smith SN (1993) Corrosion 49:114
31. Sardisco JB, Wright WB, Greco EC (1963) Corrosion 19:354
32. Sardisco JB, Pitts RE (1965) Corrosion 21:350
33. Sardisco JB, Pitts RE (1965) Corrosion 21:245
34. Nešić S, Nordsveen M, Nyborg R, Stangeland AJ (2003) Corrosion 59:443
35. Lee K-LJ, Nešić S (2005) CORROSION/05, paper no. 05630. NACE, Houston, TX
36. Nešić S, Nordsveen M, Nyborg R, Stangeland AJ (2003) Corrosion 59:489
37. Ramanarayanan TA, Smith SN (1990) Corrosion 46:66
38. Mishra B, Al-Hassan S, Olson DL, Salama MM (1997) Corrosion 53:852
39. Videm K, Kvarekvaal J, Perez T, Fitzsimons G (1998) CORROSION/98, paper no. 1. NACE, Houston, TX

40. Kaasa B, Ostvold T (1998) CORROSION/98, paper no. 62. NACE, Houston, TX
41. Crolet JL, Pourbaix M, Pourbaix A (1991) CORROSION/91, paper no. 22. NACE, Houston, TX
42. Brown B, Nešić S (2005) CORROSION/05, paper no. 05625. NACE, Houston, TX
43. Sun W, Nešić S, Papavinasam S (2008) Corrosion 64:586
44. Brown B, Parakala SR, Nešić S (2004) CORROSION/04, paper no. 04736. NACE, Houston, TX
45. Ikeda A, Ueda M, Mukai S (1985) Advances in CO_2 corrosion, vol 2. NACE, Houston, TX, pp 1–22
46. Schmitt G, Engels D (2005) CORROSION/98, paper no. 149. NACE, Houston, TX
47. Hausler RH, Gaddart HP, Advances in CO_2 corrosion, vols 1 (1985) and 2 (1986). NACE, Houston, TX
48. Videm K, Kvarekvaal J (1995) Corrosion 51:260
49. Nešić S, Lee KJ (2002) CORROSION/02, paper no. 131. NACE, Houston, TX
50. Yin ZF, Zhao WZ, Bai ZQ, Feng YR, Zhou WJ (2008) Electrochim Acta 53:3690
51. Murata T, Matsuhashi R, Taniguchi T, Yamamoto K (1979) Offshore technology conference, paper no. 3507
52. Lichti KA, Soylemezoglu S, Cunliffe KD (1981) Proceedings of the New Zealand geothermal workshop '81, paper no. 103
53. Smith JS, Miller JDA (1975) Br Corros J 10:136
54. Valdes A, Case R, Ramire ZM, Rui ZA (1988) CORROSION/98, paper no. 22. NACE, Houston, TX
55. Svenningsen G, Palencsar A, Kvarekval J (2009) CORROSION/09, paper no. 09359. NACE, Houston, TX
56. Bazan JC, Harrison JA, Staikov G, Schmidt E, Juttner K, Lorenz WJ (1988) Electrochim Acta 34:1271
57. Titz J, Wagner GH, Spahn H, Juttner K, Lorentz WJ (1990) Corrosion 46:221
58. Ernst P, Earnshaw A, Wadsworth IP, Marshall GW (1997) Corros Sci 39:1329
59. Boukamp BA (2004) Solid State Ionics 176:1959
60. Boukamp BA (1997) Equivalent circuit. University of Twente, Twente, NL
61. Shirley DA (1972) Phys Rev 135:4709
62. Heuer JK, Stubbins JF (1999) Corros Sci 41:1231
63. Sosa E, Cabrera-Sierra R, Rincon ME, Oropeza MT, Gonzáleza I (2002) Electrochim Acta 47:1197
64. Sosa E, Cabrera-Sierra R, Oropeza MT, Hernández F, Casillas N, Tremont R, Cabrera C, Gonzáleza I (2003) J Electrochem Soc 150:B530
65. Bhargava G, Gouzman I, Chun CM, Ramanarayanan TA, Bernasek SL (2007) Appl Surf Sci 253:4322
66. Wu SL, Cui ZD, He F, Bai ZQ, Zhu SL, Yang XJ (2004) Mater Lett 58:1076
67. López DA, Schreiner WH, de Sánchez SR, Simison SN (2004) Appl Surf Sci 236:77
68. Tang Z, Hong S, Xiao W, Taylor J (2006) Corros Sci 48:322
69. Moulder JF, Stickle WF, Sobol PE, Bomben KD (1992) Handbook of X-ray photoelectron spectroscopy. Perkin-Elmer, Physical Electronics Division
70. Thomas JE, Jones CF, Skinner WM, Smart RSC (1998) Geo Cosmchim Acta 62:1555
71. Brundle CR, Chuang TJ, Wandelt K (1977) Surf Sci 68:459
72. Thomas JE, Skinner WM, Smart RSC (2003) Geo Cosmchim Acta 67:831
73. Li Y, van Santen RA, Weber Th (2008) J Solid State Chem 181:151
74. Kim C-Y, Escuadro AA, Bedzyk MJ (2007) Surf Sci 601:4966
75. Prasad J, Murray E, Kelber JA (1993) Surf Sci 289:10
76. Gruzalski GR, Zehner DM, Wendelken JF (1985) Surf Sci 159:53